CHEMISTRY OF MATERIALS

pubs.acs.org/cm

Article

Environmental and Thermal Stability of Chemically Exfoliated Li_xMoS_2 for Lithium–Sulfur Batteries

Ziwei Jeffrey Yang, Zhuangnan Li,* Giulio I. Lampronti, Jung-In Lee, Yan Wang, Jason Day, and Manish Chhowalla*

Cite This: *Chem. Mater.* 2024, 36, 4829–4837

Read Online

ACCESS | Metrics & More | Article Recommendations | Supporting Information

ABSTRACT: Molybdenum disulfide (MoS_2) can exist in the semiconducting (2H) or metallic (1T) phase. The metallic 1T phase of MoS_2 is achieved by lithium intercalation using *n*-butyllithium. The resulting 1T MoS_2 can be in a lithiated form (Li_xMoS_2) or as pure MoS_2. The 1T phase of MoS_2 is metastable and relaxes to the stable 2H phase upon heating. Here we study the thermal and environmental stabilities of metallic phase Li_xMoS_2 and pure 1T phase MoS_2 for comparison. We find that the thermal stability of 1T MoS_2 is enhanced by lithiation so that Li_xMoS_2 is phase stable up to 400 °C in argon, while nonlithiated MoS_2 relaxes to the 2H phase above 150 °C. The stability of the Li_xMoS_2 was monitored under ambient conditions (23 °C, 50% relative humidity). We find that the Li_xMoS_2 phase progressively oxidizes up to 48 h of exposure in the ambient after which further oxidation ceases. X-ray diffraction shows that oxidation occurs via loss of sulfur and the formation of lithium molybdate (Li_2MoO_4). Our analysis reveals that moisture is the primary cause of oxidation and that the 1T phase and chemistry of Li_xMoS_2 can be preserved in a dry oxygen-rich environment at up to 250 °C. This enhanced stability allows the use of a conventional molten diffusion method for cathode preparation for lithium–sulfur batteries.

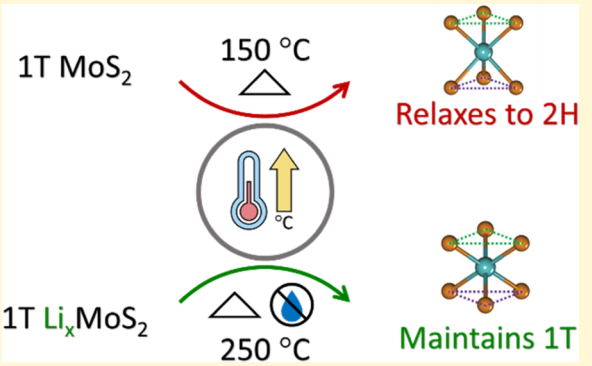

INTRODUCTION

Molybdenum disulfide (MoS_2) is a transition metal dichalcogenide (TMD) that can exist in the thermodynamically stable semiconducting hexagonal (2H) or metastable metallic tetragonal (1T) phase.[1,2] Alkali ion intercalation is typically used to transform MoS_2 from the 2H to the 1T phase.[2,3] In this technique, MoS_2 powder is dispersed in a reducing agent, such as *n*-butyllithium (*n*-BuLi) solution. The electron transfer from the butyl molecule to the d-orbital of Mo in MoS_2 balanced by intercalated lithium (or other alkali) counterions destabilizes the 2H phase in favor of 1T to form metallic lithiated MoS_2 (Li_xMoS_2).[4] After phase transformation, Li_xMoS_2 is typically washed with deionized (DI) water, during which time the intercalated alkali ions are removed, leaving behind the 1T phase MoS_2.

Due to its superior conductivity, MoS_2 in its metallic 1T phase has been shown to possess good catalytic and energy storage properties.[3,5,6] For example, 1T MoS_2 is catalytically active for the hydrogen evolution reaction (HER) even on its entire basal plane, while only the edges are catalytically active for HER in 2H MoS_2.[4,5] 1T Li_xMoS_2 is also a catalyst for the sulfur reduction reaction (SRR) as well as an excellent conductive host for sulfur.[7] However, the 1T phase in MoS_2 is metastable and can convert back to the semiconducting 2H phase after annealing.[8−10] Previous studies suggest 1T phase properties are lost after 60 days under ambient conditions,[11] and the 1T to 2H phase transformation occurs at temperature as low as 97 °C.[12] Previous efforts to stabilize the 1T phase have involved doping,[13] hydrogenation,[14] and substrate engineering.[15,16]

Here we find that the lithiated 1T Li_xMoS_2 is phase stable up to 400 °C in argon (Ar) and begins to oxidize in the presence of moisture at room temperature after 1 h. We also find that the Li_xMoS_2 phase is stable in a dry oxygen environment up to 250 °C. We study the mechanism of oxidation with X-ray diffraction (XRD) and demonstrate Li_xMoS_2 Li–S batteries with a specific energy density of 1489 mAh g^{-1}.

RESULTS AND DISCUSSION

Lithium (Li) intercalation into MoS_2 using an *n*-BuLi solution leads to transformation from the semiconducting 2H to the 1T metallic Li_xMoS_2 phase. Dispersion in different solvents via sonication exfoliates Li_xMoS_2 into single-layered nanosheets.

Received: March 7, 2024
Revised: April 9, 2024
Accepted: April 10, 2024
Published: April 19, 2024

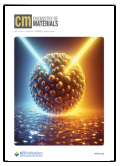

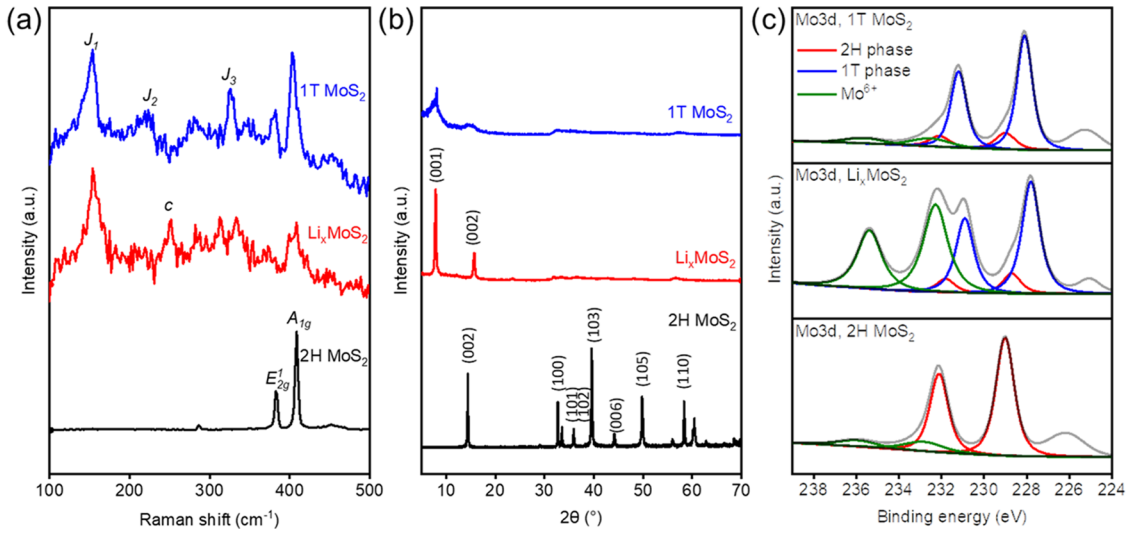

Figure 1. Material characterization of 1T MoS_2 and Li_xMoS_2 nanosheets in comparison to bulk 2H MoS_2. (a) Raman spectra showing E_{2g}^1 (in-plane; 382 cm^{-1}) and A_{1g} (out-of-plane; 406 cm^{-1}) peaks, 1T features (J_1, J_2, and J_3 peaks at 153, 220, and 325 cm^{-1}) and c peak at 250 cm^{-1}. (b) XRD patterns showing a new (001) peak at 7.8°, suggesting 2H to 1T phase transformation and an increase in interlayer spacing. (c) Deconvoluted high-resolution Mo 3d XPS spectra, showing ~74% 1T phase concentration for 1T MoS_2 nanosheets, and ~79% for Li_xMoS_2 nanosheets.

Dispersing Li_xMoS_2 in polar protic solvents, such as DI water, removes the intercalated Li ions to obtain metallic 1T MoS_2 nanosheets.[4,5,10] Dispersing Li_xMoS_2 in polar aprotic tetrahydrofuran (THF) will retain the Li ions and form Li_xMoS_2 nanosheets.[7] After the solvent is removed via freeze-drying or vacuum filtration, 1T MoS_2 or Li_xMoS_2 nanosheets are obtained.

Raman spectroscopy is used routinely to characterize MoS_2.[11,17,18] Raman spectrum of 2H MoS_2 in Figure 1a shows the characteristic E_{2g}^1 (in-plane; 382 cm^{-1}) and A_{1g} (out-of-plane; 406 cm^{-1}) peaks.[18,19] The presence of J_1, J_2, and J_3 peaks at 153, 220, and 325 cm^{-1}, respectively, are typical of the 1T phase MoS_2.[11,18] The J_2 peak in Li_xMoS_2 is weak and has been attributed to disorder at 1T and 2H grain boundaries.[14] Thus, a suppressed J_2 indicates completion of the phase transformation. An additional c peak located at 250 cm^{-1} is present in the Raman spectra of Li_xMoS_2 and is attributed to the out-of-plane interactions between sulfur (S) and intercalated lithium when the lithium-to-molybdenum (n_{Li}:n_{Mo}) ratio is >1.[20] We used inductively coupled plasma mass spectrometry (ICP-MS) and identified the n_{Li}:n_{Mo} ratio to be 2.8 (Experimental Methods) in the Li_xMoS_2 nanosheet samples. We found that the 1T phase is thermodynamically favored when n_{Li}:n_{Mo} is greater than 0.4,[21,22] and the excess Li ions are assumed to improve the 1T phase concentration, as suggested by the suppressed E_{2g}^1 intensity.[4]

X-ray diffraction (XRD) was used to identify changes in the crystal structure induced by Li intercalation and chemical exfoliation (Figure 1b). The (001) peak at 7.8° and its second-order Bragg reflection (002) at 15.6° emerge in the 1T MoS_2 and Li_xMoS_2 nanosheets. The new peaks are attributed to interlayer expansion and phase transformation caused by Li intercalation,[23] which increases the interlayer spacing from 0.62 nm in 2H MoS_2 to about 1.13 nm in 1T MoS_2 and Li_xMoS_2 nanosheets. The (001) and (002) peaks for 1T MoS_2 nanosheets are broad and less sharp due to the lack of a preferred orientation, which is a consequence of the freeze-drying process used to remove water. All other XRD features are diminished in freeze-dried 1T MoS_2 and Li_xMoS_2 nanosheet samples.

The phase of MoS_2 samples was identified using X-ray photoelectron spectroscopy (XPS) core spectra of Mo 3d, S 2p, and Li 1s (Figures 1c and S1).[18] The 1T phase concentration is ~79% for Li_xMoS_2 nanosheets and ~74% for the nonlithiated MoS_2 control sample. In Li_xMoS_2 nanosheets, a strong presence of Mo^{6+} is also identified. This contrasts with the 2H MoS_2 and 1T MoS_2 nanosheets, where the presence of Mo^{6+} is not significant and suggests low degrees of oxidation.

We first investigated the thermal phase stability of 1T MoS_2 and Li_xMoS_2 nanosheets by annealing at 150, 250, and 400 °C under Ar. We used Raman spectroscopy to identify phases of MoS_2 (Figure 2a) and Li_xMoS_2 (Figure 2b) nanosheets after annealing and modulated differential scanning calorimetry (MDSC) to measure the heat flow associated with phase transformations and other thermal events. Thermal gravimetric analysis (TGA) was used to measure the mass loss of the nanosheets during annealing (Figure 2c).

Both MoS_2 and Li_xMoS_2 nanosheets exhibit endothermic peaks in their respective MDSC curves. This is attributed to the evaporation of interlayer water and residual solvent (e.g., THF) molecules, resulting in the mass loss of 10−15% (Figure 2c). The loss of 1T phase Raman features (J_1, J_2, J_3 peaks) and the presence of an exothermic peak starting from 112 °C in MDSC suggest 1T to 2H phase transformation (Figure 2a). Density function theory (DFT) calculations have suggested that 1T to 2H phase transformation is exothermic,[24] which has been confirmed by experiments.[12] The Raman spectra of MoS_2 annealed above 150 °C are similar to that of the 2H phase and remain unchanged at higher annealing temperatures. In contrast, Li_xMoS_2 nanosheets remain in the 1T phase at 150 °C, as indicated by Raman scattering (Figure 2b). At 250 °C, the previously suppressed in-plane E_{2g}^1 peak of Li_xMoS_2 nanosheets increases in intensity. The weakened c peak also suggests a loss of interaction between Li and layered sulfur. An endothermic peak starting from 175 °C in the MDSC curve suggests that the change in the Raman spectrum originates

https://doi.org/10.1021/acs.chemmater.4c00674
Chem. Mater. 2024, 36, 4829−4837

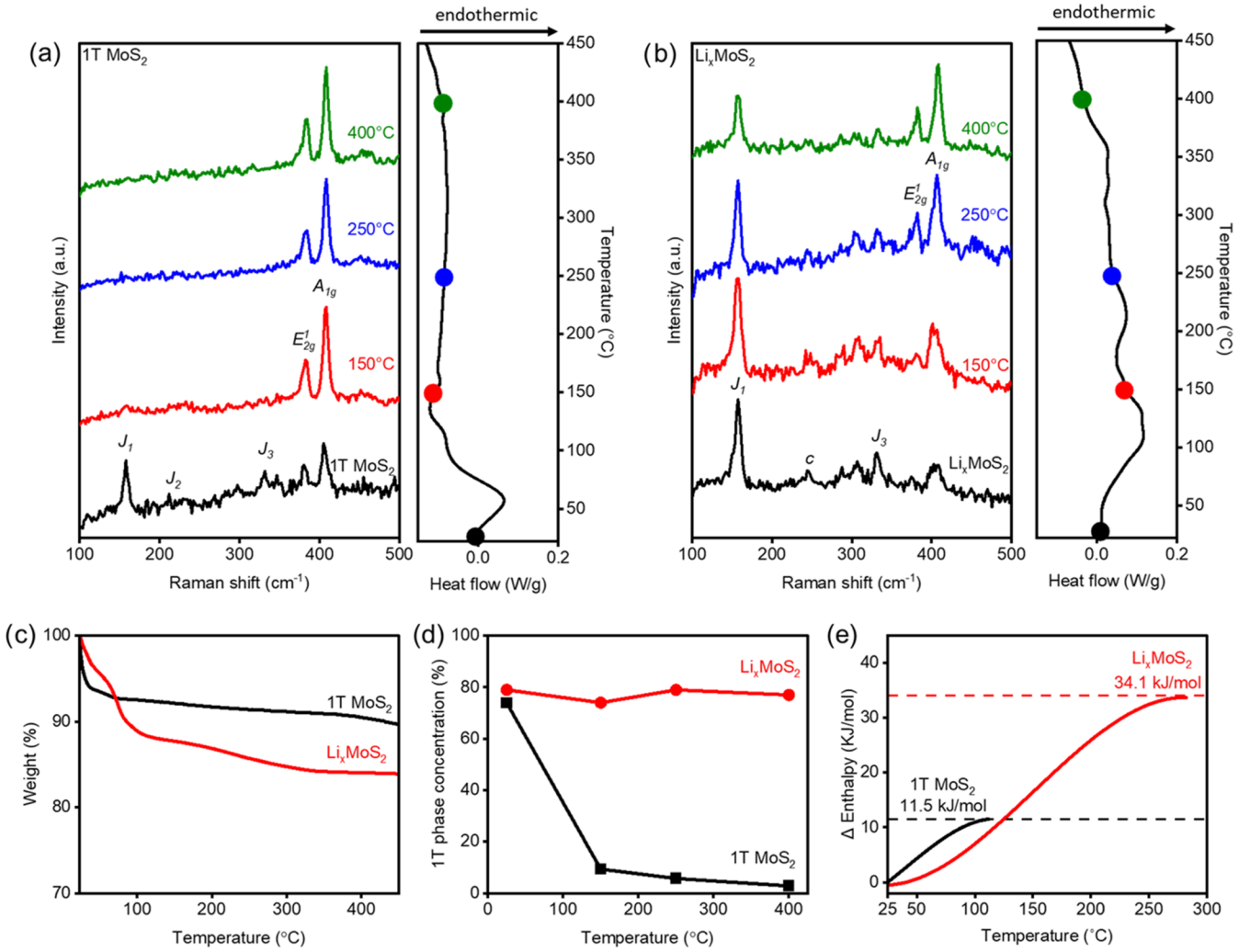

Figure 2. Thermal phase stability of 1T MoS_2 and Li_xMoS_2 nanosheets after annealing at 150, 250, and 400 °C for 60 min under Ar. (a), (b) Respective Raman spectra of MoS_2 and Li_xMoS_2 nanosheets taken at various annealing temperatures and the corresponding MDSC curve, showing loss of 1T features after 150 °C for 1T MoS_2, and presence of 1T features at 400 °C for Li_xMoS_2. (c) TGA measurements for MoS_2 and Li_xMoS_2 nanosheets, showing an initial mass loss of 10−15% due to solvent evaporation. (d) Phase quantification from XPS peak deconvolution of MoS_2 and Li_xMoS_2 nanosheets as a function of annealing temperature, showing >70% 1T phase concentration for Li_xMoS_2 at 400 °C. (e) Total change in enthalpy before the phase transformation (1T MoS_2) or sulfur sublimation (Li_xMoS_2).

from Li deintercalation.[25] The exothermic dip with an onset at 282 °C in the MDSC curve is attributed to the formation of other chemical species, likely lithium sulfide (Li_2S) from deintercalated Li and partially sublimated sulfur. The sudden change in material heat capacity and the intense endothermic nonreversing heat peak (Figure S2) provide evidence of sulfur sublimation and Li_2S formation starting at 282 °C.

The phase composition after annealing was obtained by X-ray photoelectron spectroscopy (XPS) (Figure 2d). After annealing at 150 °C, the 1T phase concentration decreased from 75 to 9% in the nonlithiated MoS_2, while the 1T phase concentration of Li_xMoS_2 remained greater than 70%, even at 400 °C (Figure S3). This suggests that after partial sulfur sublimation and Li_2S formation, the material has excess Li (n_{Li}:n_{Mo} = 2.8:1) to compensate for Li loss and retain the 1T structure.[26,27] We also calculated the total enthalpy change associated with phase transformation or sulfur sublimation by integrating the MDSC curve from room temperature (25 °C) to the respective temperatures (Figure 2e). The total enthalpy needed to bring MoS_2 nanosheets to their phase transformation temperature of 112 °C is 11.5 kJ mol^{-1} or 0.12 eV per MoS_2. The total enthalpy needed to bring Li_xMoS_2 nanosheets to their sulfur sublimation temperature of 282 °C is 34.1 kJ mol^{-1} or 0.35 eV per Li_xMoS_2. This suggests that Li_xMoS_2 is inherently more thermally stable than the nonlithiated 1T MoS_2.

We then studied the oxidation behavior under ambient conditions (23 °C and 50% relative humidity) as a function of time with in situ XRD (Figure 3a,b) and XPS (Figure 3c,d). The relative peak intensities from in situ XRD are indicators of material quantity (Experimental Methods). The (001) peak position for Li_xMoS_2 in its XRD pattern remains constant with the exposure time. This suggests a constant (001) interlayer spacing as Li_xMoS_2 ages in the ambient (Figure S4). Additional XRD peaks appear when Li_xMoS_2 is exposed to the ambient. The (012) and (12$\bar{1}$) peaks are attributed to the formation of lithium molybdate (Li_2MoO_4) as shown in Figure S5 (Li_2MoO_4, PDF 01-070-8448 reference peaks comparison).[28] The formation of Li_2MoO_4 is surprising and suggests that it is sulfur that reacts with air rather than lithium. Previous reports

https://doi.org/10.1021/acs.chemmater.4c00674
Chem. Mater. 2024, 36, 4829−4837

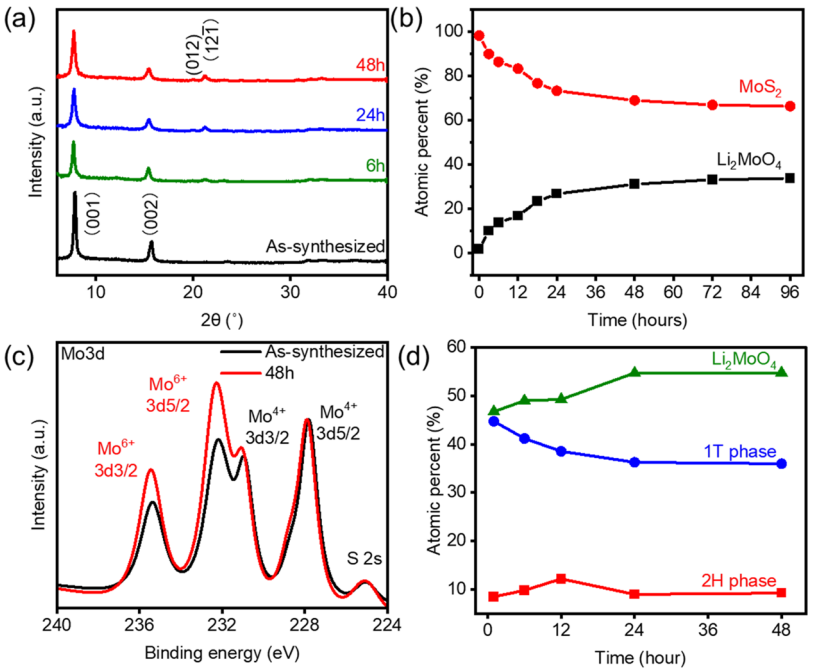

Figure 3. Identification and quantification of Li_2MoO_4 with respect to aging time under ambient conditions (23 °C and 50% relative humidity). (a) XRD patterns for as-synthesized Li_xMoS_2 and after 6, 24, and 48 h of aging. While all XRD patterns retained the (001) and (002) peaks, additional peaks (012) and (12$\bar{1}$) from Li_2MoO_4 are observed after aging. (b) Rietveld quantification of Li_2MoO_4 and MoS_2 as a function of time. Estimated standard deviations are smaller than the symbols themselves. The physical meaning of such estimated standard deviations is discussed in the Supporting Information. (c) Overlaid Mo 3d XPS spectra of as-synthesized Li_xMoS_2 nanosheets and after 48 h of aging, normalized to the Mo^{4+} $3d_{5/2}$ peak intensity. The peak intensities for Li_2MoO_4 (Mo^{6+}) at 232.5 and 235.6 eV increase with aging time. (d) Surface quantification of Li_2MoO_4, 1T, and 2H phase MoS_2 from Mo 3d XPS peak deconvolution as a function of time.

have not identified this oxidation product as Li_2MoO_4.[9,10,14,15] Rietveld quantification shows that the formation of Li_2MoO_4 is rapid in the first 12 h and then slows to a plateau after 48 h (Figure 3b). Li_2MoO_4 accounts for 1.8% of the as-synthesized Li_xMoS_2 XRD signal, which increased to ∼17% after 12 h of aging, before plateauing at 31% at 48 h. In comparison, no oxide signal was observed in the XRD pattern for nonlithiated 1T MoS_2 after 96 h of aging in ambient conditions (Figure S6).

The degree of oxidation was analyzed using XPS spectra. The XPS results from as-synthesized and Li_xMoS_2 exposed to the ambient for 48 h are included in Figure 3c, which shows the peak doublet of Mo^{6+} at 232.5 and 235.6 eV. The intensities of these peaks are noticeably higher after ambient air exposure. Deconvolution of the Mo 3d XPS spectra from as-synthesized Li_xMoS_2 nanosheets reveals that the Li_2MoO_4 contributes to 47% of the signal (Figures 3d and S7), which is much higher than the 1.8% value obtained from XRD quantification (Figure 3b). This indicates that surface oxidation is more severe than that in the bulk. Li_2MoO_4 concentration increases with exposure time and the 1T phase MoS_2 concentration decreases, while the 2H phase concentration was low and did not change with exposure time. This is consistent with Raman spectra measured with increasing exposure time to ambient (Figure S8) and suggests that the lithiated 1T phase directly converts to Li_2MoO_4 and does not phase transform to the 2H phase.[9,11,15,18]

The oxidation of Li_xMoS_2 was analyzed with transmission electron microscopy (TEM) and selected-area electron diffraction (SAED). As-synthesized Li_xMoS_2 can be seen to have a thin, disordered layer at the edge and a crystalline inner region based on SAED (Figure 4a). After aging in the ambient for 48 h, the disordered layer expands to 25 nm in width (Figure 4b), and the inner region displays a mixture of crystalline and disordered SAED pattern. XPS depth profiling was used to determine the oxidation depth and direction. It was found that the Mo^{6+} peak doublet resulting from oxidation decreases in intensity below the surface (Figures 4c and S9). Figure 4d illustrates the concentration of oxidation and the 1T phase from XPS peak deconvolution with depth.

To determine the mechanism for the oxidation of Li_xMoS_2, we exposed it for 48 h in <0.1% relative humidity dry room and 50% relative humidity ambient. XRD patterns in Figure 5a show that Li_xMoS_2 exposed to ambient humidity exhibits characteristic peaks of Li_2MoO_4, while the sample exposed to dry air remains as pristine Li_xMoS_2. Raman results (Figure 5b) also confirm the presence of J_1 (153 cm^{-1}), J_3 (325 cm^{-1}), and the c peak (250 cm^{-1}), as well as the suppression of J_2 and E_{2g}^1 peaks in the dry air exposed sample. While the Li_xMoS_2 exposed to humid air also shows J_1 and J_3 peaks, the absence of the c peak suggests a loss of excess intercalated Li due to the formation of Li_2MoO_4. We found that even in an oxygen-rich environment (∼20% oxygen), Li_xMoS_2 is both phase (Figure S10) and chemically (Figure S11) stable at 250 °C. In humid air, however, Li_xMoS_2 relaxes to the 2H phase below 150 °C (Table S1 and S2). Our results indicate that moisture is the cause of oxidation, and a possible reaction for the oxidation of Li_xMoS_2 in humid air is

$$Li_xMoS_2 + H_2O + O_2 \rightarrow Li_2MoO_4 + H_2S \quad (1)$$

We now examine Li−S batteries with Li_xMoS_2 as the conducting host for sulfur. In our previous work, we found that metallic MoS_2 leads to improved polysulfide adsorption, enhanced Li^+ transport, accelerated reaction kinetics, and

https://doi.org/10.1021/acs.chemmater.4c00674
Chem. Mater. 2024, 36, 4829−4837

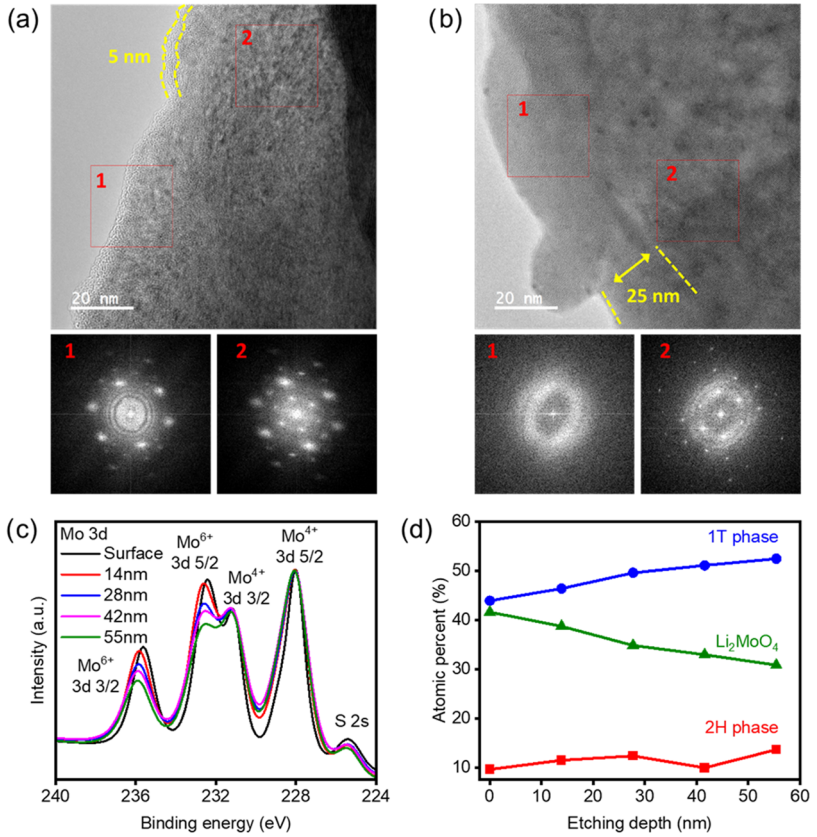

Figure 4. Li_xMoS_2 oxidation pathway characterization. (a), (b) TEM image and SAED patterns of as-synthesized and 48 h aged Li_xMoS_2. (c) Overlaid Mo 3d XPS spectra of as-synthesized Li_xMoS_2 nanosheets taken at various sample depth after ion etching. (d) Quantification of Li_2MoO_4, 1T, and 2H phase MoS_2 from Mo 3d XPS peak deconvolution with respect to probing depth.

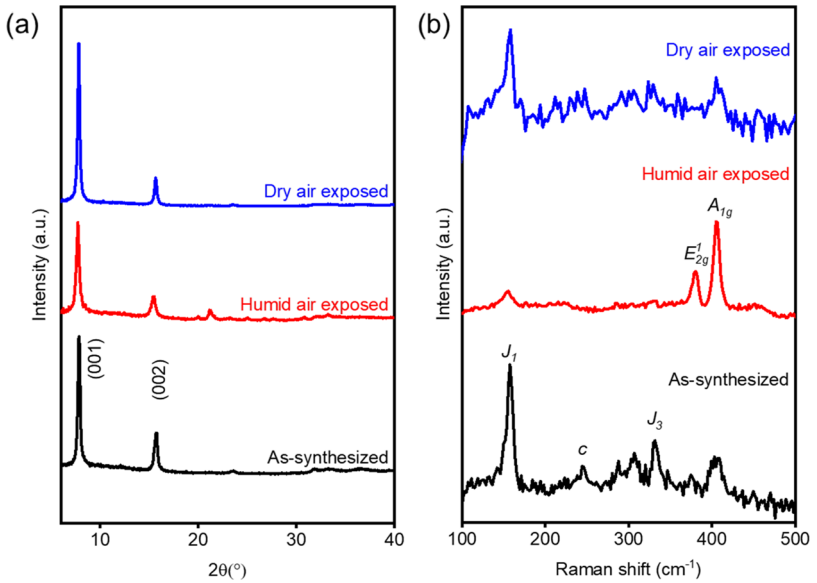

Figure 5. Comparison of (a) XRD patterns and (b) Raman spectra of as-synthesized Li_xMoS_2 nanosheets and Li_xMoS_2 exposed to dry and humid air for 48 h. Li_xMoS_2 exposed to humid air shows peaks at 19.8 and 21.1°, which are characteristic peaks of Li_2MoO_4. The Raman spectra of both samples show features unique to the 1T phase. However, the sample exposed to humid air lost intensity for J_1 and J_3 and did not retain the c peak located at 250 cm^{-1}.

superior electrocatalytic activity (Figure S12).[7] In our previous work, we used carbon disulfide (CS_2) to dissolve sulfur onto Li_xMoS_2 to avoid the relaxation of the metallic 1T phase via annealing. The present study demonstrates that upon lithiation the metallic 1T phase of Li_xMoS_2 is stable up to 250 °C in dry environments. This allows us to use the facile molten diffusion method in dry air or argon at 155 °C for cathode preparation (Experimental Methods). The as-prepared Li_xMoS_2 cathodes were assembled into coin cells, with a low areal sulfur loading (S loading) of 0.8 mg cm^{-2}, high anode-to-cathode ratio (N/

https://doi.org/10.1021/acs.chemmater.4c00674
Chem. Mater. 2024, 36, 4829−4837

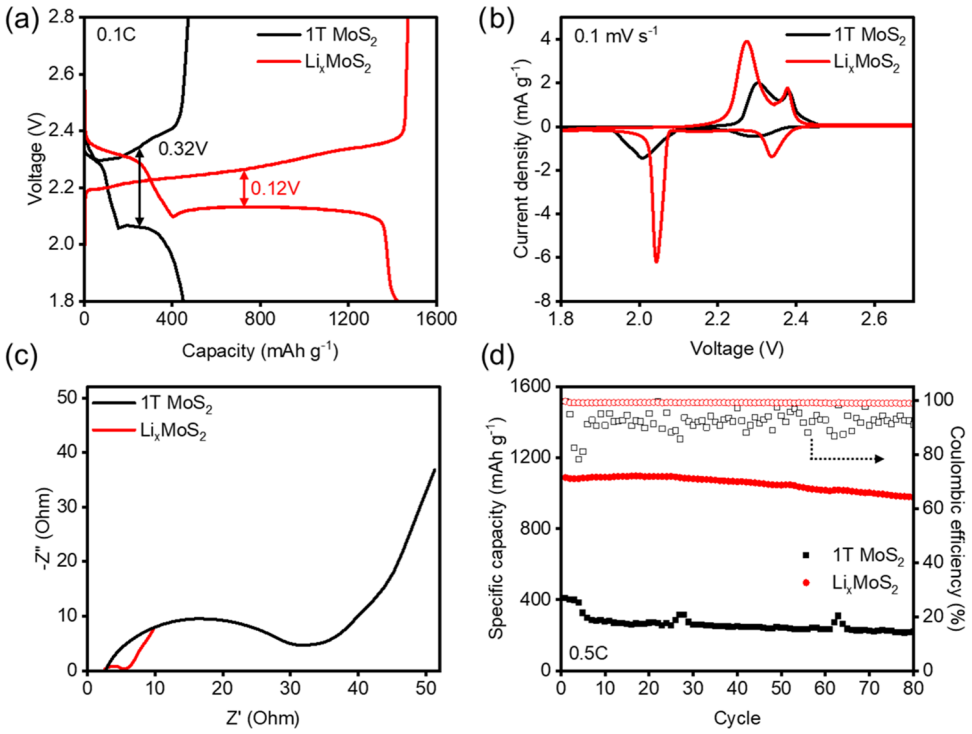

Figure 6. Electrochemical characterization of 1T MoS_2 and Li_xMoS_2 as conductive sulfur hosts in Li−S batteries. (a) GCD curves for 1T MoS_2 and Li_xMoS_2 cathodes at a current density of 0.1C. (b) CV curves for 1T MoS_2 and Li_xMoS_2 cathodes at a scan rate of 0.1 mV/s. (c) Nyquist plots for 1T MoS_2 and Li_xMoS_2 cathodes at OCV, showing the semicircular shape that represents the electrochemical impedance contributed by the electrode surface. (d) Cycle stability and Coulombic efficiency of 1T MoS_2 and Li_xMoS_2 cathodes at a current density of 0.5 C.

P), and high electrolyte-to-sulfur ratio (E/S = 30 μL mg^{-1}) to test the cathode performance. We also made pouch cells under relatively more practical conditions.

Galvanostatic charge/discharge (GCD) curves from coin cells of 1T MoS_2 and Li_xMoS_2 cathodes are shown in Figure 6a. Characteristic Li−S battery plateaus at 2.4 and 2.1 V, corresponding to the formation of liquid Li polysulfide intermediates (Li_2S_n, $3 \leq n \leq 8$), and the final reduction product Li_2S can be observed.[29,30] Due to the higher 1T phase concentration and electrical conductivity, Li_xMoS_2 cathodes (50 wt % sulfur) show a specific capacity of 1489 mAh g^{-1} at 0.1C, while the nonlithiated 1T MoS_2 cathodes possess a specific capacity of 448 mAh g^{-1} (The specific capacity is based on the mass of the active material only, when the mass of the host is included, they are 745 and 224 mAh g^{-1}, respectively). In cyclic voltammetry (CV) curves, two reduction peaks at 2.4 and 2.1 V that correspond to the plateaus in GCD curves are observed. The Li_xMoS_2 electrodes have sharper and more intense peaks than 1T MoS_2 electrodes, indicating faster reaction kinetics (Figure 6b).[29,31] This is consistent with the small voltage gap between the charge and discharge curves (0.12 vs 0.32 V), which indicates smaller ohmic loss, lower electrochemical overpotential, and favorable distribution of active sulfur.[32,33] In electrochemical impedance spectroscopy (EIS), Li_xMoS_2 electrodes display a much lower impedance at open circuit voltage (OCV), as indicated by the much smaller semicircle in the Nyquist plot shown in Figure 6c. Figure 6d and S13 (zoomed-in figure for Coulombic efficiency) also show that Li_xMoS_2 cathodes consistently maintained good Coulombic efficiency (>97%) and cycle stability, retaining 90% of the initial capacity after 80 cycles at 0.5 C, much higher than the 53% for 1T MoS_2 cathodes.

Having validated the molten diffusion method for cathode preparation in coin cells, we now demonstrate the performance of Li_xMoS_2 cathodes in a pouch cell level under realistic conditions including high S loading and low E/S and N/P ratios.[34] Areal capacity is a key metric for assessing practical energy storage systems as increasing areal capacity can reduce the overhead mass from current collectors and separators to achieve a high overall energy density. However, areal capacity does not monotonically increase with an increase in sulfur loading due to the reduced sulfur utilization rate (as indicated by specific capacity). As shown in Figure 7a, by increasing the S loading from 2.2 to 4.0 mg cm^{-2}, areal capacity increases, while the sulfur utilization rate drops from 80 to 75%. Further increasing the S loading to 6.1 mg cm^{-2} enables an areal capacity of 7.05 mAh cm^{-2} but lowers the sulfur utilization rate to 69%. The effect of the E/S ratio on the pouch cell performance is investigated in Figure 7b. At a relatively high E/S ratio of 9.7 μL mg^{-1}, pouch cells exhibit good specific capacity (1155 mAh g^{-1}) and cycling stability (~0.06% loss per cycle over 200 cycles). At a lower E/S ratio of 4.3 μL mg^{-1}, the Li_xMoS_2 cathode still retains a reasonable initial specific capacity of 1129 mAh g^{-1} despite having a more severe capacity loss of ~0.2% per cycle. We further fabricated the Li−S pouch cells at an extremely low E/S ratio of 2.1 μL mg^{-1}. The initial specific capacity reduced significantly to 930 mAh g^{-1}, and the cell failed to discharge after 82 cycles. In addition, Li_xMoS_2-based Li−S pouch cells demonstrate good rate capabilities, retaining 51% of its initial specific capacity at a relatively fast rate of 0.5 C (Figure 7c).

https://doi.org/10.1021/acs.chemmater.4c00674
Chem. Mater. 2024, 36, 4829−4837

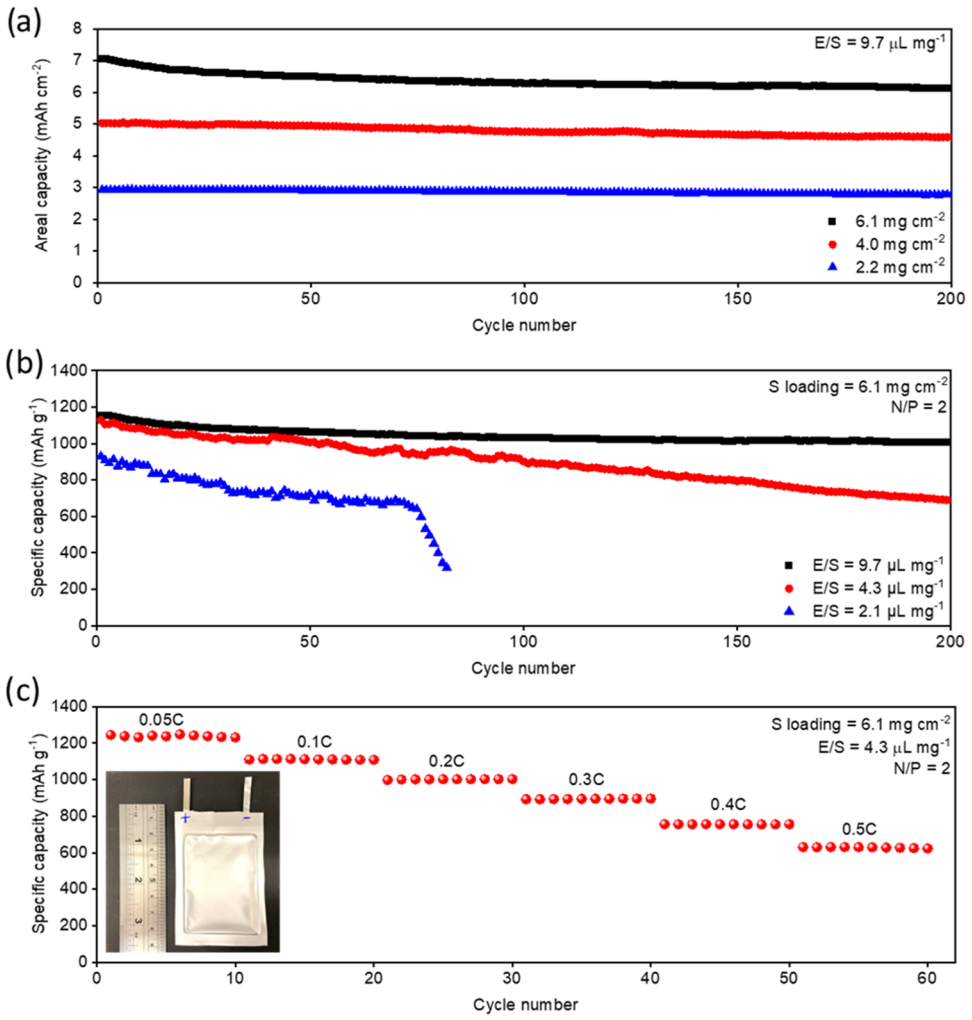

Figure 7. Pouch cell performance of Li_xMoS_2 cathodes fabricated via molten diffusion of sulfur. (a) Areal capacities of pouch cells with various sulfur loadings at a rate of 0.1C and an E/S ratio of 9.7 μL mg^{-1}. The resulting N/P ratio is between 2−5.5, depending on the sulfur loading. (b) Specific capacity of pouch cells with various E/S ratios at a rate of 0.1C, an N/P ratio of 2, and a sulfur loading of 6.1 mg cm^{-2}. (c) Specific capacities of Li_xMoS_2 pouch cell at various rates with an N/P ratio of 2, sulfur loading of 6.1 mg s^{-1}, and a E/S ratio of 4.3 μL mg^{-1}. The inset is a photograph of the Li_xMoS_2-based Li−S pouch cell (6 × 4.5 cm in dimension).

CONCLUSIONS

In summary, we have identified that Li_xMoS_2 oxidizes to form Li_2MoO_4 in humid environments and is stable in dry ambient. By retaining the Li between MoS_2 layers, Li_xMoS_2 nanosheets also exhibit thermal phase stability (250 °C in dry air), well above the 1T to 2H phase transformation temperature of 112 °C. This allows us to prepare Li−S cathodes with Li_xMoS_2 by the molten diffusion method.

EXPERIMENTAL METHODS

Preparation of Li_xMoS_2 and 1T MoS_2 Nanosheets. Li_xMoS_2 nanosheets were synthesized via liquid chemical exfoliation. Bulk 2H MoS_2 powder (0.6 g; Alfa Aesar) was immersed in hexane (30 mL; Sigma-Aldrich) under Ar. *n*-butyllithium solution (1.6 M in hexane, 6 mL; Sigma-Aldrich) was added to the mixture and refluxed for 2 days. After cooling, the product was washed with hexane (3 × 50 mL) to remove the remaining organolithium reagents and organic residues. The resultant Li_xMoS_2 powder was dispersed in tetrahydrofuran (THF) (2 mg mL^{-1}; Supelco) and ultrasonicated for 60 min in an ice bath. The Li_xMoS_2 dispersion in THF was centrifuged at 550 rpm for 210 s. The supernatant was then filtered onto an aluminum oxide membrane (0.02 μm pore size; Whatman) and dried under vacuum before it was collected as restacked nanosheets. The 1T MoS_2 nanosheets were prepared by ultrasonicating Li_xMoS_2 powder in deionized water (2 mg mL^{-1}) for 60 min in an ice bath and then centrifuging at 25,000 rpm to remove lithium cations. The settled solids were freeze-dried before they were collected as 1T MoS_2 nanosheets. 1T MoS_2 and Li_xMoS_2 aged in dry air were prepared by leaving the sample in a dry room, where the relative humidity was controlled to be <0.1%. Ar annealing was done in a tube furnace with a flow rate of 400 sccm. Ambient and dry air annealing was done in an oven in ambient or dry air.

MATERIAL CHARACTERIZATION

The materials were characterized by Raman spectroscopy (Renishaw InVia using a 514 nm laser beam), XRD (Bruker D8 Advance powder X-ray diffractometer using Cu Kα radiation, equipped with automatic divergence slits and a LynxEye-XE position sensitive detector), XPS (ThermoFisher Scientific using an Al Kα source), ICP-MS (Perkinelmer NEXION 350D), TGA (TA Instruments Discovery SDT650), MDSC (TA Instruments Q2000 DSC), and TEM (FEI Tecnai F20, 200 kV). For XRD quantitative analysis purposes, 4 mg of in-house aluminum oxide powder (Al_2O_3) reference standard was mixed to 20 mg of Li_xMoS_2 nanosheets and arranged on a silicon low background sample holder. Iterative XRD measure-

https://doi.org/10.1021/acs.chemmater.4c00674
Chem. Mater. 2024, 36, 4829−4837

ments were taken on the same sample consecutively at different degrees of oxidation without unloading the sample. Rietveld fitting was performed with TOPAS Academic V7.[35] XRD data analysis details, including preliminary structural analysis (Figure S14) of the *C*2 model of Li_xMoS_2 used for the quantitative analyses (Figure S15, Table S3), are reported in the Supporting Information. XPS depth profiling was done using Ar ion etching with an ion energy of 3000 eV and a cycle time of 5 s. The etching depth is estimated on a Ta_2O_5 reference with the same etching rate as MoS_2 at 2.73 nm s^{-1}.[36] The TEM samples were prepared by drop-casting the solution of the as-synthesis samples dispersed in THF on a copper grid supported by lacey carbon films, which were naturally dried in air and then treated under the vacuum. MDSC measurements were done between 25 and 450 °C on 2 mg of vacuum-dried Li_xMoS_2 and 1T MoS_2 nanosheets each. The average heating rate is 4 °C min^{-1}, with an amplitude of 1 °C and a period of 120 s. TGA was done on 2 mg of vacuum-dried Li_xMoS_2 and 1T MoS_2 nanosheets each, at a ramp rate of 4 °C min^{-1}. Solution for ICP-MS measurements was prepared by completely dissolving Li_xMoS_2 nanosheets with concentrated nitric acid and dilution with type 1 ultrapure DI water to a concentration of 10 ng mL^{-1}.

Coin Cell Preparation and Electrochemical Characterization. Precipitated sulfur (45 mg; Thermo Scientific) and Li_xMoS_2 or 1T MoS_2 nanosheets (45 mg) were mixed and sealed into a Teflon-lined autoclave under Ar and maintained at 155 °C for 12 h. The sulfur-MoS_2 composite was mixed with poly(vinylidene fluoride) (PVDF) (10 mg; MTI Corporation) and *N*-methyl-2-pyrrolidone (NMP) (350 mg; Sigma-Aldrich) and stirred for 24 h until a uniform slurry was achieved. The slurry was transferred to carbon-coated aluminum foil with a doctor blade to make Li_xMoS_2 or 1T MoS_2 cathodes. Thus, the materials ratio of the electrode for the coin cell is 45 wt % sulfur, 45 wt % Li_xMoS_2 or MoS_2, and 10 wt % PVDF binder. The sulfur loading was set to be about 0.8 mg cm^{-2}. The electrochemical performance of the MoS_2-based cathodes was evaluated in coin cells (CR2032), which were assembled in an Ar-filled glovebox with Li_xMoS_2/S or 1T MoS_2/S cathode, lithium foil (MTI Corporation) anode, Celgard polypropylene separator, and excess electrolyte of LiTFSI (1M; Sigma-Aldrich) and $LiNO_3$ (0.2M; Thermo Scientific) in a mixture of DOL:DME (50:50 volumetric ratio; Thermo Scientific). The electrolyte-to-sulfur ratio is controlled to be 30 μL of mg^{-1}. GCD tests were performed in the voltage range of 2.8−1.8 V at C rates = 0.1C (1C = 1672 mAh g^{-1}). The cycling stability was recorded during continuous GCD cycles at the rate of 0.5 C for 80 cycles. CV curves were scanned from 1.8 to 2.7 V and collected at a scan rate of 0.1 mV/s. EIS was measured at open circuit voltages before cycling under a sinusoidal signal over the frequency range from 100 kHz to 10 mHz with an amplitude of 10 mV.

Pouch Cell Preparation and Electrochemical Characterization. Li_xMoS_2 nanosheets and precipitate sulfur were mixed and annealed under Ar at 155 °C for 12 h at a 1:2.5 mass ratio to obtain Li_xMoS_2/S composite (71.4 wt % sulfur). The composite was then mixed with PVDF binder at a 95:5 mass ratio and made into a slurry with NMP. The slurry is coated on aluminum sheets. The areal sulfur loading is controlled to be 2.2−6.1 mg cm^{-2} by adjusting the thickness of the coating.

6 cm × 4.5 cm pouch cells (Figure 7c, inset) are assembled in a dry room (relative humidity <0.1%). The Li_xMoS_2 cathode, a Celgard polypropylene separator, and a lithium foil anode (100 μm) are stacked and packed into Al-laminated films (MTI Corporation). Al and Ni tabs (MTI Corporation) were used for the outward connection of the cathode and anode, respectively. Depending on the areal loading of the sulfur, the N/P ratio of the cell is between 2 and 5.5. The pouch cell is then transferred into an Ar-filled glovebox for the injection of electrolyte and encapsulation. The E/S ratio is controlled to be between 2.1 and 9.7 μL mg^{-1}. The pouch cells were cycled in the voltage range of 2.8−1.8 V at various rates between 0.05 and 0.5 C (1C = 1672 mAh g^{-1}).

■ ASSOCIATED CONTENT

Supporting Information

The Supporting Information is available free of charge at https://pubs.acs.org/doi/10.1021/acs.chemmater.4c00674.

Additional materials characterization, powder diffraction data analysis, structural analysis, quantitative Rietveld analysis (PDF)

Crystallographic data (ZIP)

■ AUTHOR INFORMATION

Corresponding Authors

Zhuangnan Li − *Department of Materials Science and Metallurgy, University of Cambridge, Cambridge CB30FS, U.K.*; orcid.org/0000-0001-8154-1287; Email: zl450@cam.ac.uk

Manish Chhowalla − *Department of Materials Science and Metallurgy, University of Cambridge, Cambridge CB30FS, U.K.*; orcid.org/0000-0002-8183-4044; Email: mc209@cam.ac.uk

Authors

Ziwei Jeffrey Yang − *Department of Materials Science and Metallurgy, University of Cambridge, Cambridge CB30FS, U.K.*; orcid.org/0009-0002-0442-0080

Giulio I. Lampronti − *Department of Materials Science and Metallurgy, University of Cambridge, Cambridge CB30FS, U.K.*; orcid.org/0000-0002-1430-3446

Jung-In Lee − *Department of Materials Science and Metallurgy, University of Cambridge, Cambridge CB30FS, U.K.*; orcid.org/0000-0002-5822-0722

Yan Wang − *Department of Materials Science and Metallurgy, University of Cambridge, Cambridge CB30FS, U.K.*; orcid.org/0000-0001-9241-3512

Jason Day − *Department of Earth Sciences, University of Cambridge, Cambridge CB23EQ, U.K.*

Complete contact information is available at: https://pubs.acs.org/10.1021/acs.chemmater.4c00674

Author Contributions

M.C. conceived and designed the research; Z.J.Y., Z.L., G.I.L, J.L, Y.W., and J.D. performed the experiments and the characterization of the materials; Z.J.Y., Z.L., and M.C. analyzed the data; and Z.J.Y., M.C., and Z.L. wrote the manuscript with input from all coauthors. All authors have given approval to the final version of the manuscript.

Notes

The authors declare no competing financial interest.

https://doi.org/10.1021/acs.chemmater.4c00674
Chem. Mater. 2024, 36, 4829−4837

■ ACKNOWLEDGMENTS

This report was supported by the Faraday Institution LiSTAR program and characterization project (EP/S003053/1, FIRG014, and FIRG012) and Royal Society Wolfson Merit Award (WRM\FT\180009). Z.L. acknowledges the financial support and Research Fellowship from the Herchel Smith Fund and King's College, Cambridge.

■ REFERENCES

(1) Chhowalla, M.; Liu, Z.; Zhang, H. Two-dimensional transition metal dichalcogenide (TMD) nanosheets. *Chem. Soc. Rev.* **2015**, *44*, 2584−2586.
(2) Chhowalla, M.; Shin, H. S.; Eda, G.; Li, L. J.; Loh, K. P.; Zhang, H. The chemistry of two-dimensional layered transition metal dichalcogenide nanosheets. *Nat. Chem.* **2013**, *5*, 263−275.
(3) Voiry, D.; Yang, J.; Chhowalla, M. Recent Strategies for Improving the Catalytic Activity of 2D TMD Nanosheets Toward the Hydrogen Evolution Reaction. *Adv. Mater.* **2016**, *28*, 6197−6206.
(4) Voiry, D.; Mohite, A.; Chhowalla, M. Phase engineering of transition metal dichalcogenides. *Chem. Soc. Rev.* **2015**, *44*, 2702−2712.
(5) Voiry, D.; Salehi, M.; Silva, R.; Fujita, T.; Chen, M.; Asefa, T.; Shenoy, V. B.; Eda, G.; Chhowalla, M. Conducting MoS2 nanosheets as catalysts for hydrogen evolution reaction. *Nano Lett.* **2013**, *13*, 6222−6227.
(6) Wang, H.; Zhang, Q.; Yao, H.; Liang, Z.; Lee, H. W.; Hsu, P. C.; Zheng, G.; Cui, Y. High electrochemical selectivity of edge versus terrace sites in two-dimensional layered MoS2 materials. *Nano Lett.* **2014**, *14*, 7138−7144.
(7) Li, Z.; Sami, I.; Yang, J.; Li, J.; Kumar, R. V.; Chhowalla, M. Lithiated metallic molybdenum disulfide nanosheets for high-performance lithium−sulfur batteries. *Nat. Energy* **2023**, *8*, 84−93.
(8) Lai, Z.; He, Q.; Tran, T. H.; Repaka, D. V. M.; Zhou, D.-D.; Sun, Y.; Xi, S.; Li, Y.; Chaturvedi, A.; Tan, C.; et al. Metastable 1T′-phase group VIB transition metal dichalcogenide crystals. *Nat. Mater.* **2021**, *20*, 1113−1120.
(9) Guo, Y.; Sun, D.; Ouyang, B.; Raja, A.; Song, J.; Heinz, T. F.; Brus, L. E. Probing the Dynamics of the Metallic-to-Semiconducting Structural Phase Transformation in MoS2 Crystals. *Nano Lett.* **2015**, *15*, 5081−5088.
(10) Liu, F.; Zou, Y.; Tang, X.; Mao, L.; Du, D.; Wang, H.; Zhang, M.; Wang, Z.; Yao, N.; Zhao, W.; et al. Phase Engineering and Alkali Cation Stabilization for 1T Molybdenum Dichalcogenides Monolayers. *Adv. Funct. Mater.* **2022**, *32*, No. 2204601.
(11) Jiménez Sandoval, S.; Yang, D.; Frindt, R. F.; Irwin, J. C. Raman study and lattice dynamics of single molecular layers of MoS2. *Phys. Rev. B* **1991**, *44*, 3955−3962.
(12) Yu, Y.; Nam, G.-H.; He, Q.; Wu, X.-J.; Zhang, K.; Yang, Z.; Chen, J.; Ma, Q.; Zhao, M.; Liu, Z.; et al. High phase-purity 1T′-MoS2- and 1T′-MoSe2-layered crystals. *Nat. Chem.* **2018**, *10*, 638−643.
(13) Enyashin, A. N.; Yadgarov, L.; Houben, L.; Popov, I.; Weidenbach, M.; Tenne, R.; Bar-Sadan, M.; Seifert, G. New Route for Stabilization of 1T-WS2 and MoS2 Phases. *J. Phys. Chem. C* **2011**, *115*, 24586−24591.
(14) Tan, S. J. R.; Abdelwahab, I.; Ding, Z.; Zhao, X.; Yang, T.; Loke, G. Z. J.; Lin, H.; Verzhbitskiy, I.; Poh, S. M.; Xu, H.; et al. Chemical Stabilization of 1T′ Phase Transition Metal Dichalcogenides with Giant Optical Kerr Nonlinearity. *J. Am. Chem. Soc.* **2017**, *139*, 2504−2511.
(15) Chae, S.; Chae, S. S.; Choi, M.; Park, Hm.; Chang, H.; Lee, J.-O.; Il Lee, T. Blocking of the 1T-to-2H phase transformation of chemically exfoliated transition metal disulfides by using a "lattice lock. *Nano Energy* **2019**, *56*, 65−73.
(16) Zhang, T.; Yang, T.; Qu, G.; Huang, S.; Cao, P.; Gao, W. Phase control and stabilization of 1T-MoS2 via black TiO2− nanotube arrays supporting for electrocatalytic hydrogen evolution. *J. Energy Chem.* **2022**, *68*, 71−77.
(17) Sun, Y.; Yin, S.; Peng, R.; Liang, J.; Cong, X.; Li, Y.; Li, C.; Wang, B.; Lin, M.-L.; Tan, P.-H.; et al. Abnormal Out-of-Plane Vibrational Raman Mode in Electrochemically Intercalated Multilayer MoS2. *Nano Lett.* **2023**, *23*, 5342−5349.
(18) Eda, G.; Yamaguchi, H.; Voiry, D.; Fujita, T.; Chen, M.; Chhowalla, M. Photoluminescence from Chemically Exfoliated MoS2. *Nano Lett.* **2011**, *11*, 5111−5116.
(19) Ng, H. K.; Abutaha, A.; Voiry, D.; Verzhbitskiy, I.; Cai, Y.; Zhang, G.; Liu, Y.; Wu, J.; Chhowalla, M.; Eda, G.; Hippalgaonkar, K. Effects Of Structural Phase Transition On Thermoelectric Performance in Lithium-Intercalated Molybdenum Disulfide (LixMoS2). *ACS Appl. Mater. Interfaces* **2019**, *11*, 12184−12189.
(20) Julien, C.; S, T.; Balkanski, M. Lattice dynamics of lithium intercalated MoS2. *Solid State Ionics* **1991**, *48*, 225−229.
(21) Enyashin, A. N.; Seifert, G. Density-functional study of LixMoS2 intercalates (0⩽x⩽1). *Comput. Theor. Chem.* **2012**, *999*, 13−20.
(22) Kan, M.; Wang, J. Y.; Li, X. W.; Zhang, S. H.; Li, Y. W.; Kawazoe, Y.; Sun, Q.; Jena, P. Structures and Phase Transition of a MoS2Monolayer. *J. Phys. Chem. C* **2014**, *118*, 1515−1522.
(23) Acerce, M.; Voiry, D.; Chhowalla, M. Metallic 1T phase MoS2 nanosheets as supercapacitor electrode materials. *Nat. Nanotechnol.* **2015**, *10*, 313−318.
(24) Ryzhikov, M. R.; Slepkov, V. A.; Kozlova, S. G.; Gabuda, S. P.; Fedorov, V. E. Solid-state reaction as a mechanism of 1T ↔ 2H transformation in MoS2 monolayers. *J. Comput. Chem.* **2015**, *36*, 2131−2134.
(25) Wang, M.; Xu, Y. H.; Lu, F.; Zhu, Z.; Dong, J. Y.; Fang, D. L.; Zhou, J.; Yang, Y. J.; Zhong, Y. T.; Chen, S. M.; et al. Enhanced Li-Ion-Storage Performance of MoS2 through Multistage Structural Design. *ChemElectroChem.* **2019**, *6*, 1475−1484.
(26) Liu, R.; Li, X.; Jia, Z.; Wang, Y.; Peng, Y.; Tang, C.; Chen, Z.; Dong, L. Sulfur Vacancy-Rich MoS2-Catalyzed Hydrodeoxygenation of Lactic Acid to Biopropionic Acid. *ACS Sustainable Chem. Eng.* **2022**, *10*, 5463−5475.
(27) Cai, L.; He, J.; Liu, Q.; Yao, T.; Chen, L.; Yan, W.; Hu, F.; Jiang, Y.; Zhao, Y.; Hu, T.; et al. Vacancy-Induced Ferromagnetism of MoS2 Nanosheets. *J. Am. Chem. Soc.* **2015**, *137*, 2622−2627.
(28) Kolitsch, U. The crystal structures of phenacite-type Li2(MoO4), and scheelite-type LiY(MoO4)2 and LiNd(MoO4)2. *Z. Kristallogr. - Cryst. Mater.* **2001**, *216*, 449−454.
(29) Manthiram, A.; Fu, Y. *Advances in Rechargeable Lithium-Sulfur Batteries*; Springer: Cham, 2022.
(30) Manthiram, A.; Fu, Y.; Chung, S. H.; Zu, C.; Su, Y. S. Rechargeable lithium-sulfur batteries. *Chem. Rev.* **2014**, *114*, 11751−11787.
(31) Manthiram, A.; Chung, S.-H.; Zu, C. Lithium-Sulfur Batteries: Progress and Prospects. *Adv. Mater.* **2015**, *27*, 1980−2006.
(32) Van Der Ven, A.; See, K. A.; Pilon, L. Hysteresis in electrochemical systems. *Battery Energy* **2022**, *1*, No. 20210017.
(33) Li, L.; Jacobs, R.; Gao, P.; Gan, L.; Wang, F.; Morgan, D.; Jin, S. Origins of Large Voltage Hysteresis in High-Energy-Density Metal Fluoride Lithium-Ion Battery Conversion Electrodes. *J. Am. Chem. Soc.* **2016**, *138*, 2838−2848.
(34) Bhargav, A.; He, J.; Gupta, A.; Manthiram, A. Lithium-Sulfur Batteries: Attaining the Critical Metrics. *Joule* **2020**, *4*, 285−291.
(35) Coelho, A. A. TOPAS and TOPAS-Academic: an optimization program integrating computer algebra and crystallographic objects written in C++. *J. Appl. Crystallogr.* **2018**, *51*, 210−218.
(36) Sputtering Yields. Angstrom Sciences 2013 https://angstromsciences.com/sputtering-yields/(accessed 2023−11−24).

https://doi.org/10.1021/acs.chemmater.4c00674
Chem. Mater. 2024, 36, 4829−4837